

# A probabilistic framework for acoustic emission source localization in plate-like structures

E Dehghan Niri and S Salamone

Smart Structures and Research Laboratory, Department of Civil Structural and Environmental Engineering, State University of New York at Buffalo (UB), NY 14260, USA

E-mail: [ssalamon@buffalo.edu](mailto:ssalamon@buffalo.edu)

Received 18 August 2011, in final form 15 December 2011

Published 10 February 2012

Online at [stacks.iop.org/SMS/21/035009](http://stacks.iop.org/SMS/21/035009)

## Abstract

This paper proposes a probabilistic approach for acoustic emission (AE) source localization in isotropic plate-like structures based on an extended Kalman filter (EKF). The proposed approach consists of two main stages. During the first stage, time-of-flight (TOF) measurements of Lamb waves are carried out by a continuous wavelet transform (CWT), accounting for systematic errors due to the Heisenberg uncertainty; the second stage uses an EKF to iteratively estimate the AE source location and the wave velocity. The advantages of the proposed algorithm over the traditional methods include the capability of: (1) taking into account uncertainties in TOF measurements and wave velocity and (2) efficiently fusing multi-sensor data to perform AE source localization. The performance of the proposed approach is validated through pencil-lead breaks performed on an aluminum plate at systematic grid locations. The plate was instrumented with an array of four piezoelectric transducers in two different configurations.

(Some figures may appear in colour only in the online journal)

## 1. Introduction

In the past two decades, significant effort has been made towards the development of structural health monitoring (SHM) systems based on guided ultrasonic waves (GUWs) in order to increase safety and performance of aircraft systems [1–3]. Damage events, both on ground and in-flight, can represent a threat to aircraft systems. Sources of damage include hail impact, lightning strike, transport and handling, and foreign objects. Techniques based on sparse arrays of sensors, which have the capability of transmitting and receiving Lamb waves are among the most promising candidates. The application of Lamb waves can be challenging as they are multimode (many vibrating modes can propagate simultaneously) and dispersive (the propagation velocity depends on the wavefrequency  $f$ ). In plate-like structures two fundamental modes can propagate: symmetric (S) and antisymmetric (A). Displacements of the symmetric modes occur in the direction of wave propagation

(i.e. extensional modes), whilst antisymmetric modes have displacements transverse to the wave propagation direction (i.e. flexural modes). Damage location using Lamb waves, can be achieved by either an ‘active–passive’ approach or by a ‘passive-only’ approach. In the ‘active–passive’ approach, diffractions of piezoelectrically actuated waves can be used to locate existing damage in a post-mortem mode [4, 5]. In the ‘passive-only’ approach, growing damage or sudden impacts can be located by monitoring acoustic emissions in a real-time mode [6–12]. This paper, focus on a ‘passive-only’ approach using a sparse array of piezoelectric transducers.

Traditionally, damage or impact location is based on time-of-flight (TOF) triangulation of wave measurements taken at multiple receiving points. This technique works very well when the wave velocity ( $V_g$ ) in the test material and the arrival time ( $t_i$ ) of the signal at all three sensor locations are known. The damage or impact location is identified by drawing three circles of radii ( $R_i$ ), whose centers coincide with the three sensor locations. The radius  $R_i$  is obtained

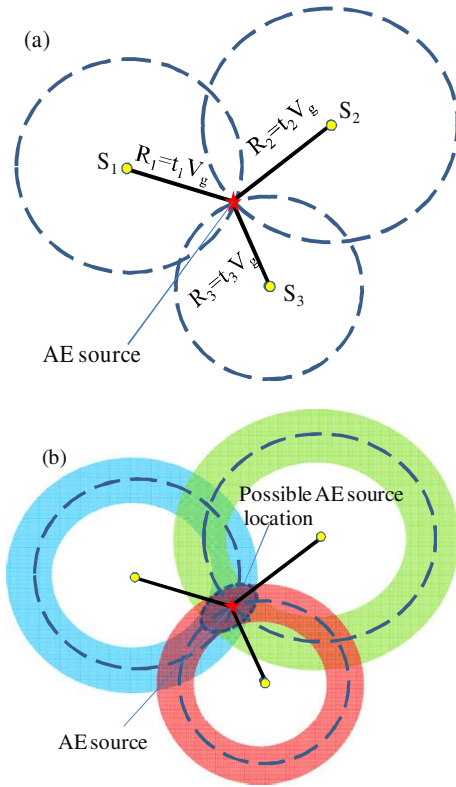


**Figure 1.** AE source localization using triangulation (a) without uncertainty and (b) with uncertainty.

by multiplying the time of arrival of the signal ( $t_i$ ) with the wave velocity ( $V_g$ ). The intersection point of these three circles is the damage location (figure 1(a)). However, TOF and wave velocity are two uncertain parameters. In general, uncertainties can be caused by random and systematic errors. The random errors are caused by unknown and unpredictable changes in the TOF measurements, including instrumentation noise, temperature changes etc [13–18]. Systematic errors are mostly caused by the digital signal processing technique used for analyzing the time waveforms [19]. As a result, rather than the damage being located at a single point at the intersection of the circles as in figure 1(a), the damage can be located anywhere in the dark overlapped region in figure 1(b). Model-based approaches [20] have been proposed for impact location and identification in simple structures. In these methods the location and type of impact in a model are iteratively changed until the predicted responses match the measured responses. For damage/impact location in more complex structures, where accurate model-based predictions may not be possible, artificial neural networks have been proposed [21, 22]. However, neural networks require an extensive number of training observations prior to deployment, making these methods quite onerous from a computational or data storage point of view. Kundu *et al* [7], proposed an alternative method based on optimizing an objective function to find the impact location in isotropic and anisotropic plate. However, the proposed objective function in that reference had the inherent problem of multiple

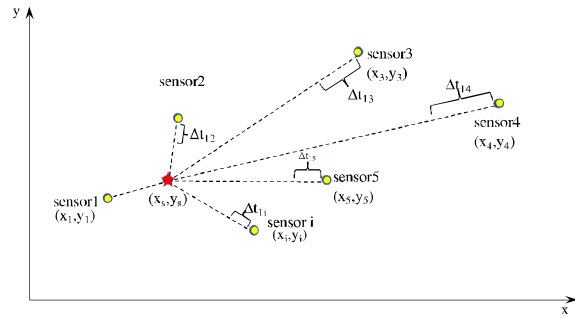


**Figure 2.** AE source location and sparse array of  $n$  piezoelectric sensors.

singularities which was overcome in Kundu *et al* [23] by modifying the objective function. The optimization technique was further improved by Hajzargerbashi *et al* [24]. In [25] and [26] the nonlinear least square optimization adopting the Gauss–Newton method was proposed to determine the location, time lag, and velocity of ‘synthetic’ AE signals. Ciampa and Meo [12] used Newton’s iterative method to calculate the coordinates of the impact location and the wave velocity. A genetic algorithm (GA) for optimization of an objective function based on the modified triangulation methodology was proposed in [27].

Here an alternative probabilistic approach, based on the extended Kalman filter (EKF) theory, is proposed for AE source localization and wave velocity identification in isotropic plate-like structures. This approach, in which TOF and wave velocity are considered as Gaussian random variables, consists of two main stages. During the first stage, TOF measurements of Lamb waves are carried out by a continuous wavelet transform (CWT) accounting for systematic errors due to the Heisenberg uncertainty; the second stage uses the EKF to iteratively estimate the location of the AE source and the wave velocity. The paper begins by briefly introducing the algorithm for the AE source localization. Section 3 summarizes the main characteristics of the CWT for TOF and frequency measurements. This is followed by section 4 which briefly introduces the EKF theory. In section 5, the AE source location based on the EKF shall be discussed. Section 6 reports the experimental setup followed by the results in section 7. Finally, the conclusions are given in section 8.

## 2. Source location algorithm

Assuming an arbitrary Cartesian coordinate system, the AE source is at unknown coordinates  $(x_s, y_s)$  in the plane of the plate and the sensors are located at  $(x_i, y_i)$ , as shown in figure 2. It is well known that given the wave velocity of a particular Lamb wave mode, at least three sensors are necessary to locate an AE source in plate-like structures. If  $t_m$  is the travel time to reach the first sensor (master sensor), and  $\Delta t_{mi}$  are the time difference between master sensor and the  $i$ th sensor, the following equations can be obtained:

$$(x_m - x_s)^2 + (y_m - y_s)^2 - (t_m V_g)^2 = 0 \quad (2.1)$$

$$(x_i - x_s)^2 + (y_i - y_s)^2 - [(t_m + \Delta t_{mi})V_g]^2 = 0 \quad (2.2)$$

where  $V_g$  is the group velocity of the particular Lamb wave mode, which is a function of the product of the frequency  $f$  and the plate thickness  $d$ :

$$V_g = F(fd). \quad (2.3)$$

Knowing the properties of the plate, mass density  $\rho$ , thickness  $d$ , Young's modulus  $E$ , and Poisson ratio  $\nu$ ,  $V_g$  can be calculated by the Rayleigh–Lamb equations [28]. Combining equations (2.1) and (2.2) the following equation can be derived:

$$\Delta t_{mi} = \frac{\sqrt{(x_i - x_s)^2 + (y_i - y_s)^2} - \sqrt{(x_m - x_s)^2 + (y_m - y_s)^2}}{V_g}. \quad (2.4)$$

In general, the differences between the TOF of the master sensor to different sensors ( $\Delta t_{mi}$ ) are used to solve this set of nonlinear equations with unknowns  $\mathbf{X} = (x_s, y_s, V_g)$ . However, as mentioned in section 1, several sources of error in the TOF measurements (i.e. dispersion, noise, temperature, etc), can affect the accuracy of this solution. In this work, to take into account uncertainties in the arrival time or TOF  $t_i$  and the wave velocity  $V_g$ , the arrival time  $t_i$  and unknowns  $x_s, y_s, V_g$  are treated as mutually independent Gaussian random variables. Based on this assumption, the probability density function of the time difference  $\Delta t_{mi}$  can also be defined as a Gaussian random variable [29] with mean and variance defined as:

$$\Delta t_{mi} = t_i - t_m, \quad \sigma_{\Delta t_{mi}}^2 = \sigma_{t_i}^2 + \sigma_{t_m}^2. \quad (2.5)$$

Time differences  $\Delta t_{mi}$  are determined through a time–frequency analysis using a CWT which has inherent uncertainties in time and frequency localization caused by the Heisenberg inequality, as will be explained in section 3. In this probabilistic framework, an extended Kalman filter (EKF) approach is proposed in section 4 for the optimal estimation of the state vector  $\mathbf{X} = (x_s, y_s, V_g)$ .

### 3. The continuous wavelet transform (CWT)

A variety of methods for increasing the accuracy of TOF measurements of acoustic waves have been developed, including the short time Fourier transform (STFT), Wigner–Ville distribution (WVD), CWT, and Hilbert–Huang transform (HHT) [3]. In this work a CWT has been employed for its good resolution both in the time and frequency domain and for its multi-resolution property [30]. The CWT of a signal  $f(t)$  is defined as [31]:

$$\text{WT}(s, b) = \frac{1}{\sqrt{s}} \int_{-\infty}^{+\infty} f(t) \Psi^* \left( \frac{t-b}{s} \right) dt \quad (3.1)$$

where  $s > 0$  is the scale or dilatation parameter,  $b$  is the translation parameter localizing the wavelet in the time domain.  $\Psi(t)$  is called the mother wavelet, and  $\Psi^*(t)$  denotes the complex conjugate of the mother wavelet. Several researchers have used the CWT to analyze Lamb waves in

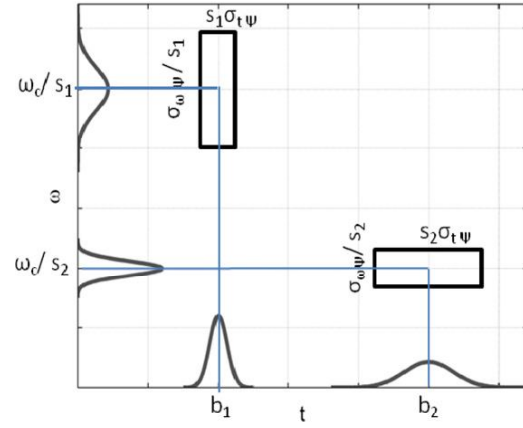


Figure 3. Time–frequency localization.

plate-like structures for AE source localization [11, 12, 25, 32]. However, in this paper a new approach is proposed to take into account systematic uncertainties, in the arrival time measurements and group wave velocity assumption, due to the Heisenberg uncertainty principle.

#### 3.1. Heisenberg uncertainty

The local resolution of the CWT in time and frequency domains is limited according to the Heisenberg inequality [31] which is defined as:

$$\sigma_t^2 \sigma_\omega^2 \geq \frac{1}{4} \quad (3.2)$$

where  $\sigma_t$  and  $\sigma_\omega$ , representing the local time and frequency resolution of the CWT, depend on the scale parameter ( $s$ ) and on the mother wavelet properties as:

$$\sigma_t = \sigma_{t\Psi} s, \quad \sigma_\omega = \frac{\sigma_{\omega\Psi}}{s}. \quad (3.3)$$

Here  $\sigma_{t\Psi}$  and  $\sigma_{\omega\Psi}$  are the standard deviations representing time and frequency resolution of the mother wavelet, defined as [31]:

$$\sigma_{t\Psi} = \frac{1}{\|\Psi\|_2} \sqrt{\int_{-\infty}^{+\infty} (t - t_\Psi)^2 |\Psi(t)|^2 dt} \quad (3.4)$$

$$\sigma_{\omega\Psi} = \frac{1}{\|\hat{\Psi}\|_2} \sqrt{\int_{-\infty}^{+\infty} (\omega - \omega_\Psi)^2 |\hat{\Psi}(\omega)|^2 d\omega} \quad (3.5)$$

where  $t_\Psi$  and  $\omega_\Psi$  are the centers of  $\Psi(t)$  and  $\hat{\Psi}(\omega)$  respectively and can be calculated by:

$$t_\Psi = \int_{-\infty}^{+\infty} t \frac{|\Psi(t)|^2}{\|\Psi\|_2^2} dt \quad (3.6)$$

$$\omega_\Psi = \int_{-\infty}^{+\infty} \omega \frac{|\hat{\Psi}(\omega)|^2}{\|\hat{\Psi}\|_2^2} d\omega. \quad (3.7)$$

Here  $\|\cdot\|_2$ , and  $|\cdot|$  denote the classical norm two and the absolute value respectively. According to equation (3.2) an improvement in time localization causes the deterioration

in frequency localization and vice versa. For some mother wavelets, such as the complex Morlet, the localization in the time and frequency domain can be represented by two Gaussian probability density functions with variance  $\sigma_t^2$  and  $\sigma_\omega^2$  and mean values of  $b + st_\psi$  and  $\frac{\omega_\psi}{s}$ , respectively. Figure 3 shows these probability density functions and their corresponding Heisenberg boxes of two wavelets  $\Psi_{b_1, s_1}(t)$  and  $\Psi_{b_2, s_2}(t)$ . In this work, the variance in time domain  $\sigma_t^2$  will be used to define the uncertainty in arrival time, and the variance in the frequency domain  $\sigma_\omega^2$  will be correlated to the uncertainty in the group wave velocity defined by the variance  $\sigma_{V_g}^2$ . It can be stated that by increasing the time resolution the systematic error in arrival time determination decreases. On the other hand, the uncertainty in the initiation of group velocity  $\sigma_{V_g}^2$ , which is related to  $\sigma_\omega^2$  through the well-known Rayleigh–Lamb equations, increases according to equation (3.2).

### 3.2. Complex Morlet wavelet

There are several mother wavelets reported in the literature and exploited to extract time and frequency information from acquired signals. In this study a complex Morlet was employed as it is able to separate amplitude and phase information, but also it achieves a desirable compromise between time and frequency resolution, with the area of the Heisenberg box equal to 0.5 [31]. The complex Morlet is defined as:

$$\Psi(t) = \frac{1}{\sqrt{\pi f_b}} e^{-\frac{t^2}{f_b}} e^{2\pi f_c t} \quad (3.8)$$

where  $f_c$  and  $f_b$  represents the center frequency and frequency bandwidth, respectively.  $f_b$  controls the shape of the mother wavelet and, for a given scale parameter  $s$ , it determines the resolution in the time and frequency domain. The following equations show the  $\sigma_t$  and  $\sigma_\omega$  in equation (3.3) for the complex Morlet [33]:

$$\sigma_t = \frac{s\sqrt{f_b}}{2}, \quad \sigma_\omega = \frac{1}{s\sqrt{f_b}}. \quad (3.9)$$

Figure 4 shows the real and imaginary part of the complex Morlet wavelet and the corresponding Gaussian distribution functions with mean  $t_\psi = 0$  and standard deviation  $\sigma_{t_\psi} = \frac{\sqrt{f_b}}{2}$  in the time domain and with mean  $\omega_\psi = 2\pi f_c$  and standard deviation  $\sigma_{\omega_\psi} = \frac{1}{\sqrt{f_b}}$  in the frequency domain. To find the arrival times a scale  $s$  should be selected, as explained in section 3.3.

### 3.3. Determining the difference of arrival time

The squared modulus of the CWT (scalogram) represents the energy density of a signal in the frequency–time domain [31]. The scalogram can be defined as:

$$|WT(s, b)|^2 = WT(s, b) \cdot WT^*(s, b) \quad (3.10)$$

where  $WT^*$  represents the conjugate of wavelet transform WT. The maximum value of the coefficients of the scalogram

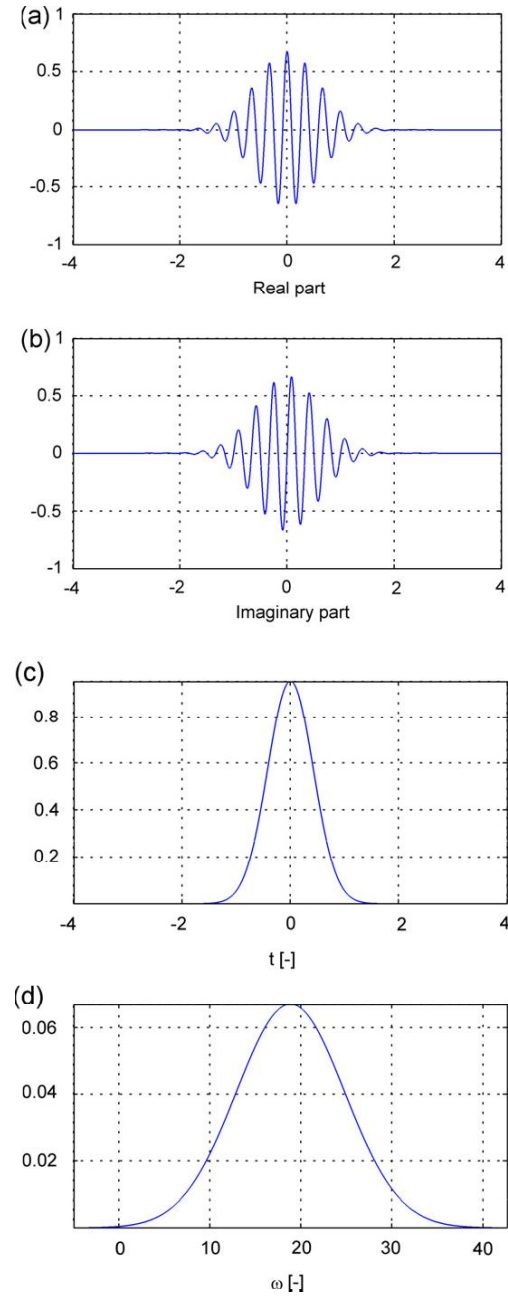


**Figure 4.** Complex Morlet wavelet (a) real part in the time domain, (b) imaginary part in time domain, (c) probability distribution function in the time domain and (d) probability distribution function in the frequency domain.

is achieved at the instantaneous frequency [11, 25, 30], corresponding to the dominant frequency in the signal analyzed at each instant in time. These coefficients, taken at the instantaneous frequency in a time–frequency domain, determine the ridges [31]. The projection of the ridge corresponding to the dominant frequency  $f_i$  represents the arrival time of the wavepacket. In this work, because the dominant frequency can be different at each sensor, the

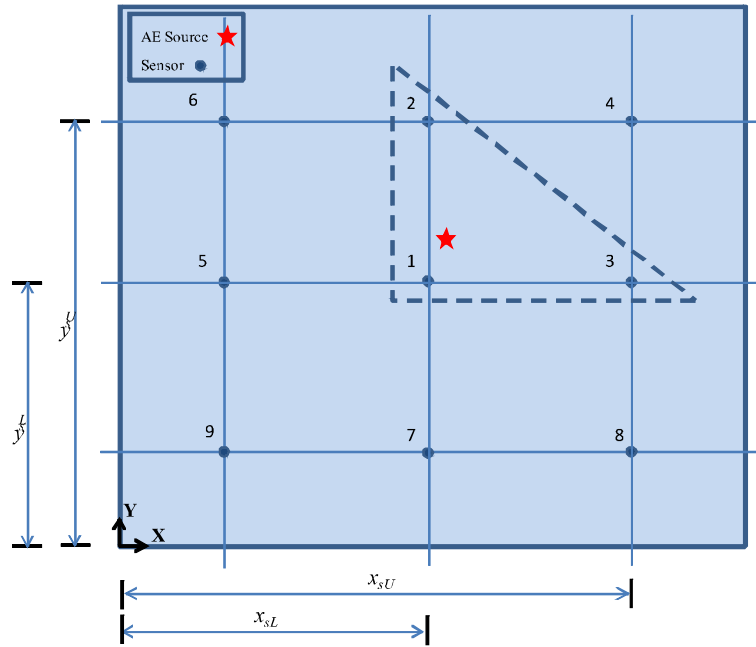


Figure 5. Network of fired sensors.

average  $\bar{f}$  is used to calculate the arrival time  $t_i$ :

$$\bar{f} = \frac{\sum_{i=1}^n f_i}{n}. \quad (3.11)$$

The corresponding scale  $\bar{s}$  is defined as:

$$\bar{s} = \frac{\omega_\psi}{2\pi\bar{f}} \quad (3.12)$$

where  $\omega_\psi$  is defined in equation (3.7) and is  $\omega_\psi = 2\pi f_c$  for the complex Morlet wavelet. By substituting equation (3.12) into (3.9),  $\sigma_t$  and  $\sigma_\omega$  for the complex Morlet wavelet can be defined as:

$$\sigma_t = \frac{f_c \sqrt{f_b}}{2\bar{f}} \quad (3.13)$$

$$\sigma_\omega = \frac{\bar{f}}{f_c \sqrt{f_b}}. \quad (3.14)$$

Substituting equation (3.13) into (2.5) the variance of the difference in arrival times  $\sigma_{\Delta t_{mi}}^2$  is defined as:

$$\sigma_{\Delta t_{mi}}^2 = 2 \left( \frac{f_c \sqrt{f_b}}{2\bar{f}} \right)^2. \quad (3.15)$$

This value is used to model the uncertainty of the measurement vector, which is given as input to the proposed EKF algorithm. For the sake of clarity a brief general derivation of the EKF theory is presented in section 4.

#### 4. Extended Kalman filter (EKF)

In general, a Kalman filter (KF) is a recursive data processing algorithm that estimates the state of a noisy dynamic system [34]. When we talk about the state of a system we

mean a vector  $\mathbf{X}$  consisting of  $n$  variables describing some interesting properties of the system. To estimate the state a KF processes all available measurements, both accurate and inaccurate measurements. The KF has been widely used in a wide range of applications due to its simplicity, optimality, robustness, sensor fusion ability and its capability in considering the uncertainties due to the mathematical model and measurements [34–37]. In general the KF is a two steps process: (1) state prediction according to a mathematical model and (2) correction of the state according to the measurements collected by sensors. More specifically, in the prediction step the KF estimates the state of the system at a given time instant and then obtains a feedback control in the correction step, by incorporating a new measurement result into the *a priori* estimate, in order to gain an improved *a posteriori* estimate. Although the underlying approach is very promising there is a critical limitation. In fact the KF assumes that system and measurements are adequately modeled by a linear dynamic system. The EKF is similar to the KF but it can be used in nonlinear systems. For this reason the EKF has been used to handle the set of nonlinear equation (2.4).

##### 4.1. EKF formulations

Without loss of generality, let us consider a generic nonlinear dynamic system with no external inputs, as follows:

$$\mathbf{X}_{k+1} = f(\mathbf{X}_k) + \mathbf{w}_k \quad (4.1)$$

$$\mathbf{Z}_k = h(\mathbf{X}_k) + \mathbf{v}_k \quad (4.2)$$

where  $\mathbf{X}_k$  is the current  $n$ -dimensional state vector of the system,  $\mathbf{Z}_k$  is the  $m$ -dimensional vector of current measurements at the  $k$ th step,  $f$  and  $h$  are known functions,



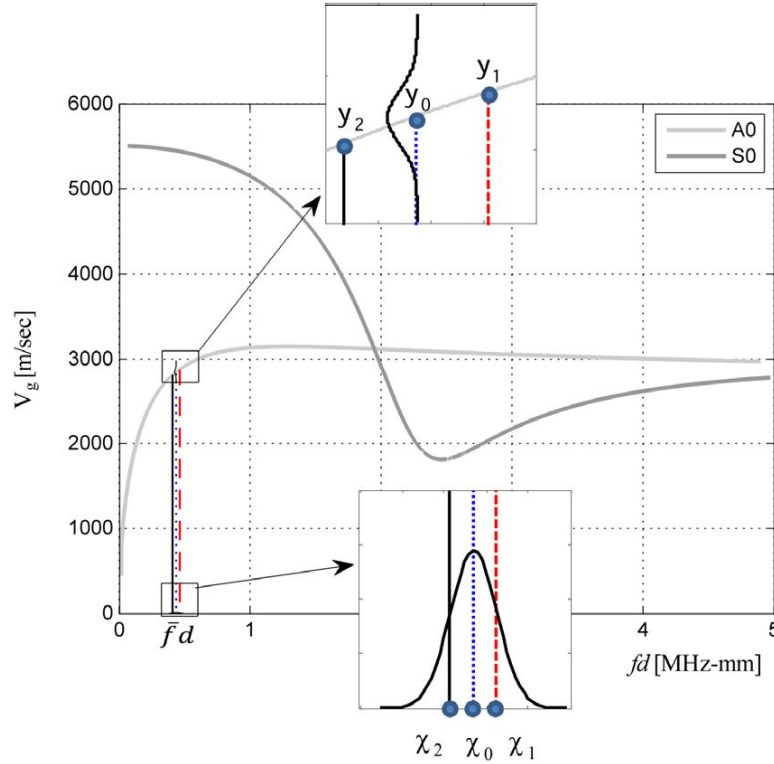


Figure 6. Unscented transformation.

and  $v_k \sim \mathcal{N}(0, \mathbf{R})$  and  $w_k \sim \mathcal{N}(0, \mathbf{Q})$  are uncorrelated noisy Gaussian processes with zero mean and covariance matrices  $\mathbf{R}$  and  $\mathbf{Q}$ . The objective is to obtain estimates  $\hat{\mathbf{X}}_k$  of the state  $\mathbf{X}_k$  using measurements  $\mathbf{Z}_k$  so that  $\text{tr}(\mathbb{E}[(\mathbf{X}_k - \hat{\mathbf{X}}_k)(\mathbf{X}_k - \hat{\mathbf{X}}_k)^T])$  is minimized (tr, E, and T denote trace, expected value, and transpose respectively). According to the EKF, the  $f$  and  $h$  functions can be approximated through the first-order Taylor series expansions with respect to  $\mathbf{X}$ . With this assumption, the prediction stage of the process may be analyzed through the following equations:

$$\hat{\mathbf{X}}_k^- = f(\hat{\mathbf{X}}_{k-1}^+) \quad (4.3)$$

$$\hat{\mathbf{P}}_k^- = \Phi_{k-1} \hat{\mathbf{P}}_{k-1}^+ \Phi_{k-1}^T + \mathbf{Q}_k \quad (4.4)$$

$$\hat{\mathbf{Z}}_k^- = h(\hat{\mathbf{X}}_k^-) \quad (4.5)$$

$$\Phi_k = \left. \frac{\partial f(\mathbf{X})}{\partial \mathbf{X}} \right|_{\mathbf{X}=\hat{\mathbf{X}}_{k-1}^+} \quad (4.6)$$

where  $\Phi_k$  is the state transition matrix.  $\hat{\mathbf{X}}_k^-$ ,  $\hat{\mathbf{P}}_k^-$ , and  $\hat{\mathbf{Z}}_k^-$  are the *a priori* (predicted) estimates of the state vector, the error covariance matrix, and the predicted measurements, respectively. The correction stage equations are expressed as:

$$\hat{\mathbf{X}}_k^+ = \hat{\mathbf{X}}_k^- + \bar{\mathbf{K}}_k(\mathbf{Z}_k - \hat{\mathbf{Z}}_k^-) \quad (4.7)$$

$$\hat{\mathbf{P}}_k^+ = (\mathbf{I} - \bar{\mathbf{K}}_k \mathbf{H}_k) \hat{\mathbf{P}}_k^- \quad (4.8)$$

where  $\mathbf{I}$  is an identity matrix;  $\hat{\mathbf{X}}_k^+$  and  $\hat{\mathbf{P}}_k^+$  are *a posterior* (corrected) estimates and the Jacobian matrix  $\mathbf{H}_k$  contains the

partial derivatives of the measurement function  $h$  with respect to the state  $\mathbf{X}$ , evaluated at the prior state estimate  $\hat{\mathbf{X}}_k^-$  and is defined as:

$$\mathbf{H}_k = \left. \frac{\partial h(\mathbf{X})}{\partial \mathbf{X}} \right|_{\mathbf{X}=\hat{\mathbf{X}}_k^-} \quad (4.9)$$

and  $\bar{\mathbf{K}}_k$  is the Kalman gain defined as follows:

$$\bar{\mathbf{K}}_k = \hat{\mathbf{P}}_k^- \mathbf{H}_k^T (\mathbf{H}_k \hat{\mathbf{P}}_k^- \mathbf{H}_k^T + \mathbf{R})^{-1} \quad (4.10)$$

The EKF has been shown to be successful in many practical nonlinear applications [34]. To the best of the authors' knowledge, none of the techniques presented in the literature for AE source location take advantage of the EKF theory.

## 5. AE source localization based on EKF

In this work, the state of the system  $\mathbf{X}$  consists of three parameters, the AE source location  $(x_s, y_s)$  and the wave velocity  $V_g$ . Given a sparse array of  $n$  sensors, the time differences  $\Delta t_{mi}$  between the  $i$ th sensor and the master sensor represent the measurement data vector  $\mathbf{Z} = [\Delta t_{mi}]_{(n-1) \times 1}$ ,  $n \geq 3$ . The state of the system  $\mathbf{X}$  is related to the measurement vector  $\mathbf{Z}$  through the nonlinear measurement function  $h$  defined in equation (2.4). The key idea underlying the proposed approach is that the AE source location can be considered as an unmovable (static) or slowly fluctuating point. Under this assumption, the prediction step of the EKF can be simplified, as the transition matrix  $\Phi_k$  reduces itself

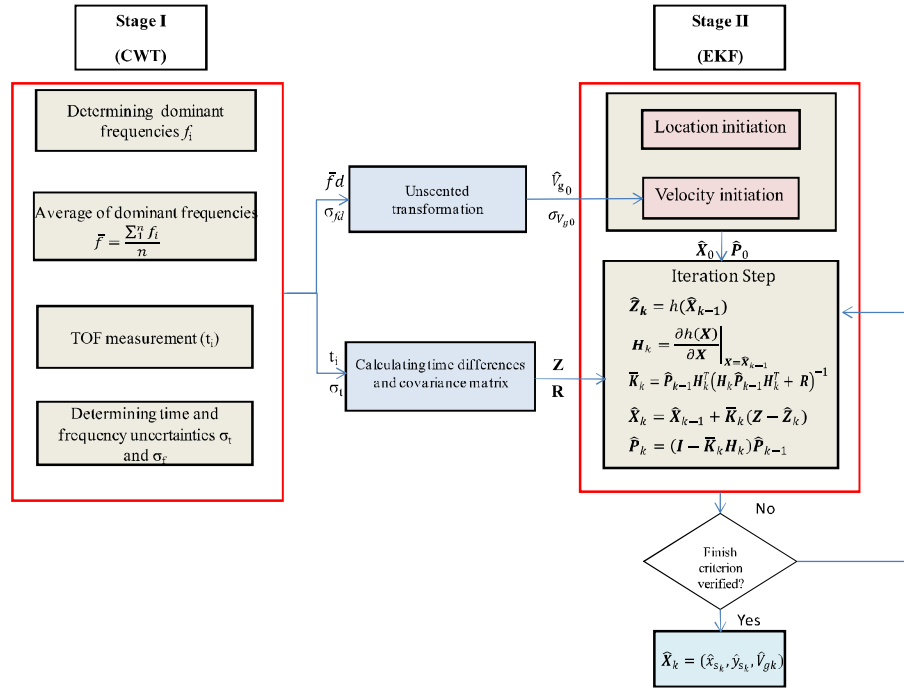


Figure 7. Proposed approach flowchart.

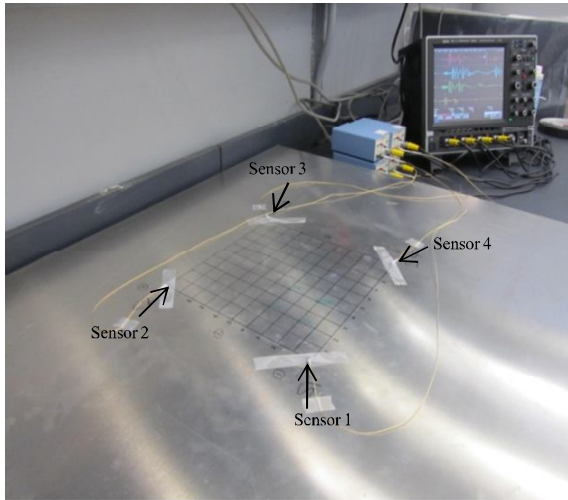


Figure 8. Experimental setup.

to the unity matrix  $I$ . Furthermore, since the state  $X$  has no superimposed noise,  $Q$  is considered to be null. Under these assumptions, the EKF algorithm can be simplified by neglecting the prediction stage. Thus the *posterior* estimation is equal to the *a priori* estimation at any step  $k$ , (i.e. the superscripts ‘-’ and ‘+’ can be neglected) and the equations (4.5), (4.7), (4.8) and (4.9) take the following forms:

$$\hat{Z}_k = h(\hat{X}_{k-1}) \quad (5.1)$$

$$\hat{X}_k = \hat{X}_{k-1} + \bar{K}_k (Z - \hat{Z}_k) \quad (5.2)$$

$$\hat{P}_k = (I - \bar{K}_k H_k) \hat{P}_{k-1} \quad (5.3)$$

$$H_k = \left. \frac{\partial h(X)}{\partial X} \right|_{X=\hat{X}_{k-1}}. \quad (5.4)$$

Also equation (4.10) can be rewritten as:

$$\bar{K}_k = \hat{P}_{k-1} H_k^T (H_k \hat{P}_{k-1} H_k^T + R)^{-1}. \quad (5.5)$$

It should be noted that the measurement vector  $Z$  in equation (5.2) does not have the subscript  $k$  because its  $(n-1)$  components (difference in arrival times) can be considered constant, once the AE signals have been acquired. Thus during the iteration to estimate the state vector  $X$  this measurement vector is constant. The uncertainty of measurement vector  $Z$  is modeled as a zero mean white Gaussian noise with covariance matrix  $R$  with diagonal terms defined in equation (3.15).

$$R = \begin{bmatrix} \sigma_{\Delta t_{m1}}^2 & \cdots & 0 \\ \vdots & \ddots & \vdots \\ 0 & \cdots & \sigma_{\Delta t_{m(n-1)}}^2 \end{bmatrix}. \quad (5.6)$$

The objective is to estimate the state vector  $X = [x_s, y_s, V_g]$  given the measurement vector  $Z$  and covariance matrix  $R$ . The EKF will iteratively correct *a priori* knowledge of the state vector  $\hat{X}$  and covariance matrix  $\hat{P}$ , with respect to the  $Z$  and  $R$ .

The iteration begins with the initialization of the state vector estimate  $\hat{X}_0$  and its covariance matrix  $\hat{P}_0$ :

$$\hat{X}_0 = [\hat{x}_{s0}, \hat{y}_{s0}, \hat{V}_{g0}] \quad \hat{P}_0 = \begin{bmatrix} \sigma_{x_{s0}}^2 & 0 & 0 \\ 0 & \sigma_{y_{s0}}^2 & 0 \\ 0 & 0 & \sigma_{V_{g0}}^2 \end{bmatrix}. \quad (5.7)$$

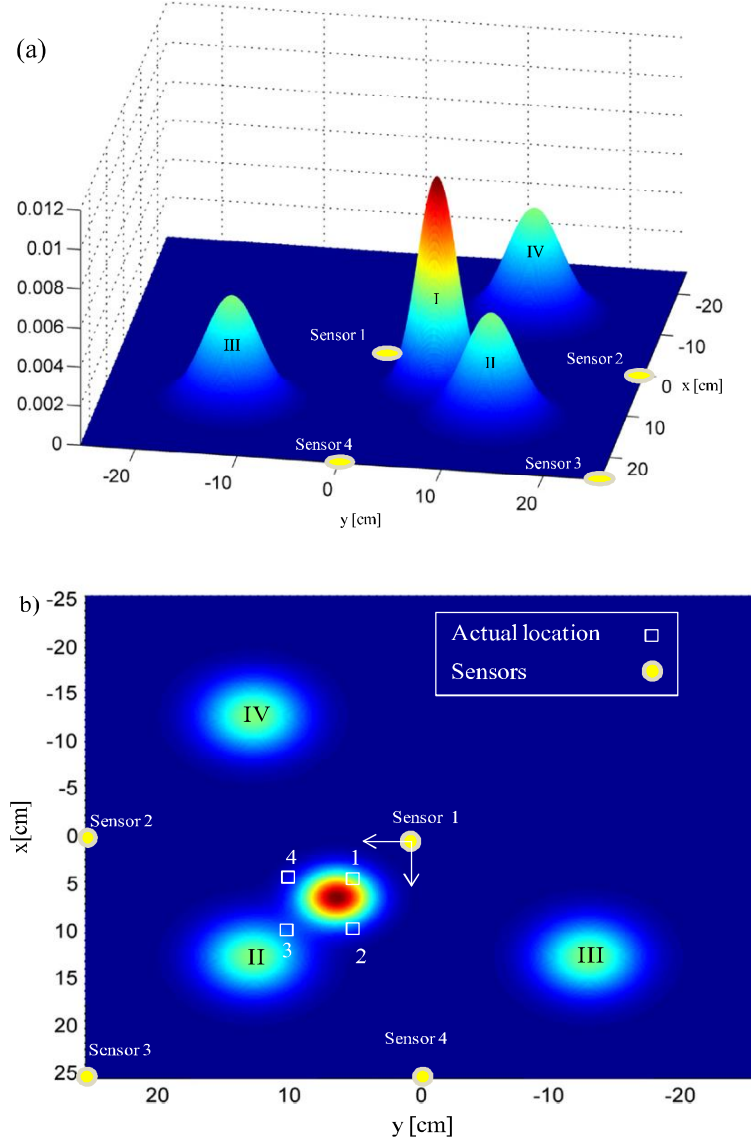


**Figure 9.** Initial Gaussian locations in the first configuration of sensors and actual locations of simulated AE sources: (a) 3D view and (b) planar view.

### 5.1. Initiation of location

The starting estimates of the AE source location  $\hat{x}_{s0}$  and  $\hat{y}_{s0}$  can be calculated by geometrical considerations. Given an arbitrary group of  $n$ -fired sensors at locations  $(x_i, y_i)$ , it can be assumed that estimated coordinates of the source location  $\hat{x}_s$  and  $\hat{y}_s$  can take any value in the intervals of  $(x_{sL}, x_{sU})$  and  $(y_{sL}, y_{sU})$ , where  $x_{sL}$  and  $y_{sL}$  are the lower bounds defined as:

$$x_{sL} = \min([x_i]_n); \quad y_{sL} = \min([y_i]_n) \quad (5.8)$$

and  $x_{sU}$  and  $y_{sU}$  are the upper bounds defined as:

$$x_{sU} = \max([x_i]_n); \quad y_{sU} = \max([y_i]_n). \quad (5.9)$$

For the sake of clarity in figure 5 is shown the simplest case of three fired sensors. Making these assumptions, mean

and variance for an uncorrelated uniform distribution can be expressed as:

$$\hat{x}_{s0} = \frac{(x_{sU} + x_{sL})}{2}, \quad \hat{y}_{s0} = \frac{(y_{sU} + y_{sL})}{2} \quad (5.10)$$

$$\sigma_{x_{s0}}^2 = \frac{1}{12} (x_{sU} - x_{sL})^2, \quad \sigma_{y_{s0}}^2 = \frac{1}{12} (y_{sU} - y_{sL})^2. \quad (5.11)$$

### 5.2. Initiation of group velocity $V_g$

In section 3 the frequency ( $f$ ) has been assumed as a Gaussian random variable with mean and variance defined in equations (3.11) and (3.14). The starting estimates of the group wave velocity  $\hat{V}_{g0}$  and its variance  $\sigma_{V_{g0}}^2$  can



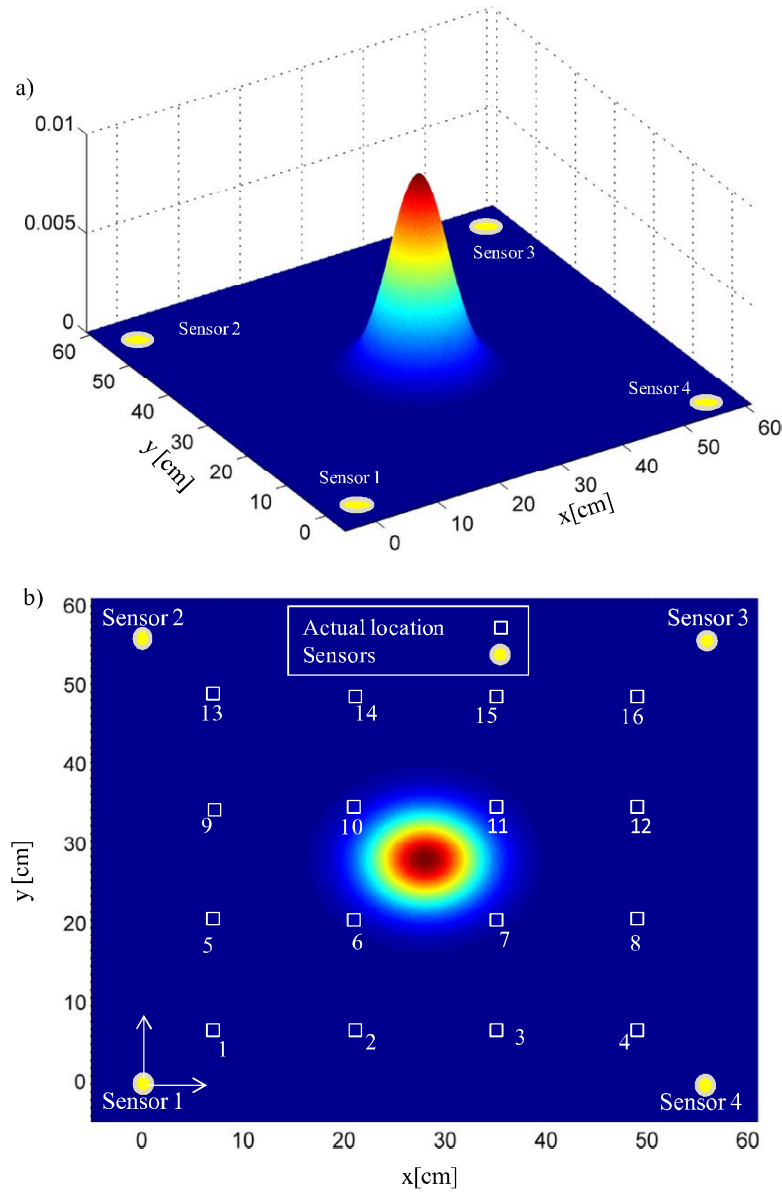


**Figure 10.** Initial Gaussian locations used in the second configuration of sensors and actual locations of generated AE sources: (a) 3D view and (b) planar view.

be calculated determining the relationship between the probability distributions of the two random variables  $f$  and  $V_g$  when they are related by  $V_g = F(fd)$ . Assuming the functional form  $F(fd)$  is given and deterministic, we are interested in determining the probability density function of  $V_g$  given the probability density function of  $f$  (the thickness of the plate  $d$  is deterministic). Because in general the functional form of  $F$  is not available, in this work an unscented transformation (UT) has been used. The UT is a method for calculating the statistics of a random variable which undergoes a nonlinear transformation [38]. Assuming the random variable  $fd$  has mean  $\bar{f}d$  and variance  $\sigma_{fd}^2$ , three weighted sigma points  $\chi_0$ ,  $\chi_1$ , and  $\chi_2$  are necessary to calculate the statistics of  $V_g$ . These

points are given by:

$$\begin{aligned} \chi_0 &= \bar{f}d, & W_0 &= \frac{\kappa}{(1+\kappa)} \\ \chi_1 &= \bar{f}d + \left( \sqrt{(1+\kappa)\sigma_{fd}^2} \right), & W_1 &= \frac{1}{2(1+\kappa)} \\ \chi_2 &= \bar{f}d - \left( \sqrt{(1+\kappa)\sigma_{fd}^2} \right)_i, & W_2 &= \frac{1}{2(1+\kappa)} \end{aligned} \quad (5.12)$$

where  $W_i$  is the weight associated with the  $i$ th point and  $\kappa$  is an arbitrary number providing  $1 + \kappa \neq 0$ ;  $\kappa = 0$  is chosen in this work. Given the set of sigma points calculated by equation (5.12), the transformation of the Gaussian probability density function of the random variable  $fd$  to the

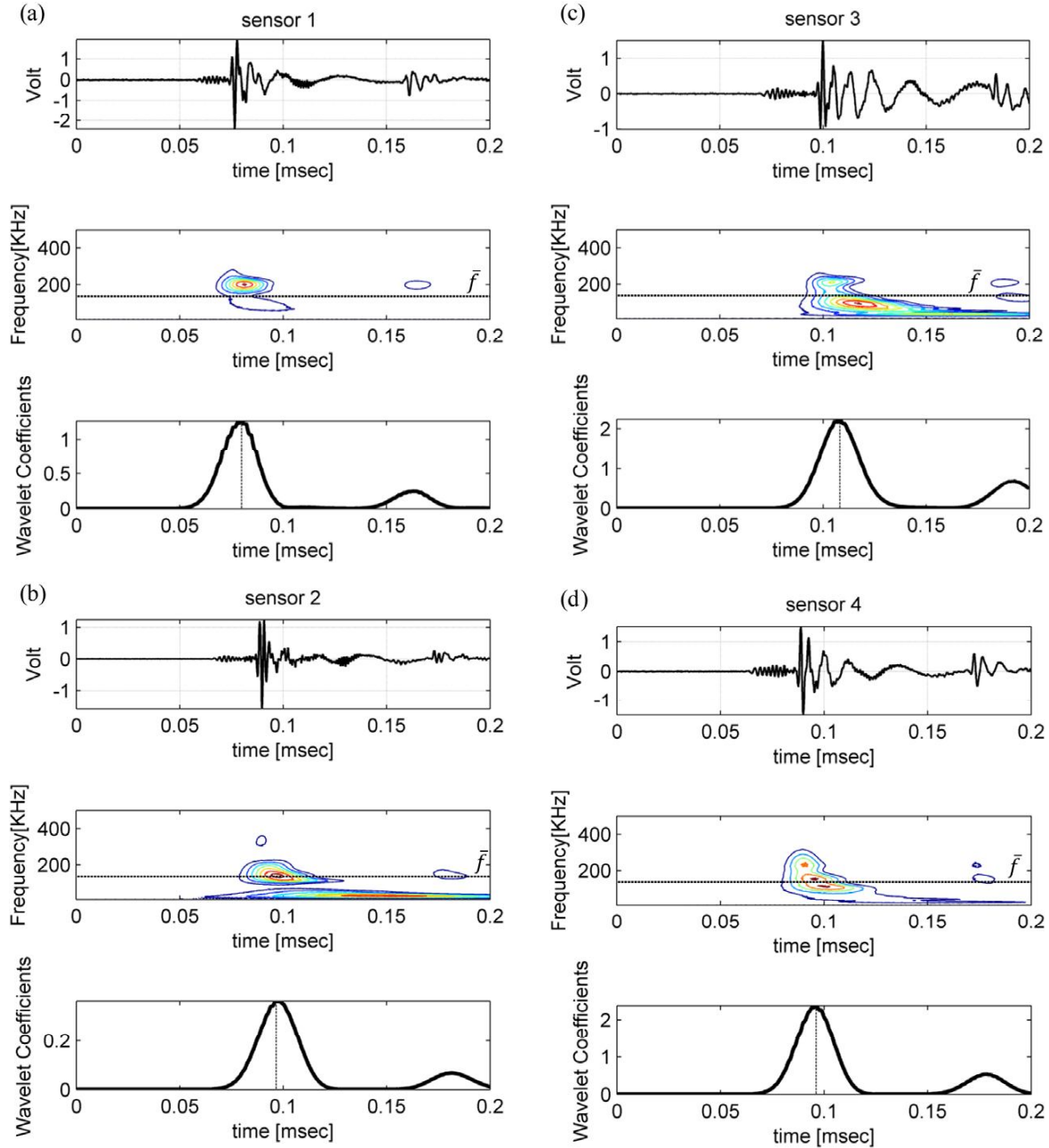


**Figure 11.** Each figure depicts the time histories of the four signals acquired by the sensors, the contour plot of the scalogram of the CWT, and the line profile of the scalogram showing the procedure to find the time of arrival at  $\bar{f} = 137.00$  kHz for AE point 4.

approximated Gaussian distribution of  $V_g$  is summarized in the following steps.

- (1) Calculate the group velocity corresponding to each sigma point according to dispersion curvature or the Rayleigh–Lamb equations.

$$\mathcal{Y}_i = F(\chi_i), \quad i = 0, 1, 2. \quad (5.13)$$

- (2) The mean of random variable  $V_g$  can be calculated from:

$$\bar{V}_g = \sum_0^2 W_i \mathcal{Y}_i. \quad (5.14)$$

- (3) The variance of random variable  $V_g$  can be determined by:

$$\sigma_{V_{g0}}^2 = \sum_0^2 W_i \{\mathcal{Y}_i - \bar{V}_g\} \{\mathcal{Y}_i - \bar{V}_g\}^T. \quad (5.15)$$

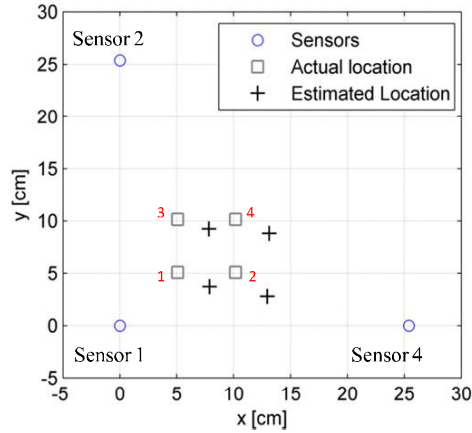


**Figure 12.** AE source localization results using three sensors in the first setup configuration.

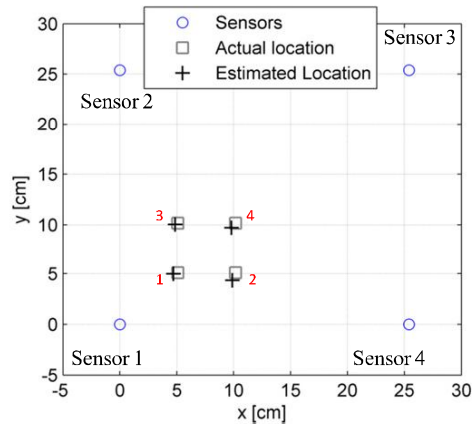


**Figure 13.** AE source localization results using four sensors in the first setup configuration.

Now the initial group wave velocity for a specified mode is  $\hat{V}_{g0} = \bar{V}_g$  and its corresponding variance used in equation (5.7) is  $\sigma_{V_{g0}}^2$ . Figure 6 shows this transformation for a given frequency  $\bar{f}$  assuming  $A_0$  as the dominant Lamb wave mode. In the appendix is presented another approach that can be used to perform this transformation in the case where the functional form of  $F$  is known. Overall, the proposed approach consists of two stages as shown in the flowchart in figure 7; the first stage provides information about time of arrivals, frequency, and their uncertainties; the second stage uses *a priori* information about the states and iteratively estimates the state vector according to the measured information obtained from the first stage.

## 6. Experimental setup

Experiments were carried out using an aluminum plate with dimensions 910 mm  $\times$  910 mm  $\times$  3.175 mm to validate the proposed algorithm. The plate was instrumented with an array of four piezoelectric transducers in two square

**Table 1.** Properties of four initial Gaussian locations.

Initial Gaussian location	I	II	III	IV
$x_{sU}$ (cm)	12.7	25.4	25.4	-25.4
$y_{sU}$ (cm)	12.7	25.4	-25.4	25.4
$\sigma_{x_s}^2$ (cm <sup>2</sup> )	13.44	53.76	53.76	53.76
$\sigma_{y_s}^2$ (cm <sup>2</sup> )	13.44	53.76	53.76	53.76
$\hat{x}_{s0}$ (cm)	6.35	12.7	12.7	-12.7
$\hat{y}_{s0}$ (cm)	6.35	12.7	-12.7	12.7

Note: The origin of Cartesian coordinates is at sensor 1.

**Table 2.** Properties of initial velocity in the first setup configuration.

Actual location	$\bar{f}$ (kHz)	$\hat{V}_{g0}$ (m s <sup>-1</sup> )	$\sigma_{V_{g0}}^2$ (m s <sup>-1</sup> ) <sup>2</sup>
1	152.75	2901.8	1063.7
2	150.00	2892.1	1076.2
3	112.25	2724.8	1612.4
4	137.00	2843.4	1258.7

configurations, with dimensions 254 mm and 560 mm, respectively. The experimental setup is shown in figure 8. For the data acquisition, a LeCroy Waverunner oscilloscope with sampling frequency of 10 MHz was used. Each sensor was connected to a preamplifier. During testing, AE sources were generated by pencil-lead breaks at systematic grid locations. To preferentially generate the antisymmetric ( $A_0$ ) Lamb wave mode the lead was fractured on the plate surface [39]. Post-processing of the received signals was performed with a PC running a Matlab software code implemented by the authors. The complex Morlet parameters were set by trial and error and fixed ( $f_c = 3$  Hz,  $f_b = 0.7$  Hz).

The first configuration was used to investigate the convergence behavior of the EKF to the initial guess,  $\hat{X}_0$  and  $\hat{P}_0$ . In particular, four initial Gaussian locations were used, as shown in figure 9. In this figure the actual source location is marked as a squared dot ( $\square$ ) and each sensor with a circle ( $\circ$ ). The lower bound  $x_{sL}$  and  $y_{sL}$  is the location of the master sensor (sensor 1) located at the origin of the coordinate system and the upper bounds  $x_{sU}$  and  $y_{sU}$  are summarized in table 1. The second configuration was used to validate the performance of the proposed approach in additional known locations. In particular, artificial AE sources were generated by pencil-lead breaks on 16 grid points. The initial Gaussian location was calculated based on equations (5.8) and (5.9) where the lower bound  $x_{sL}$  and  $y_{sL}$  is the location of the master sensor (sensor 1) located at the origin of the coordinate system and the upper bound  $x_{sU}$  and  $y_{sU}$  is the location of sensor 3. Figure 10 shows the initial Gaussian location used to perform the source localization at each point.

## 7. Results and discussion

The frequency  $\bar{f}$  of each simulated AE source, and the corresponding mean and variance of the initial group velocity computed using the UT, are summarized in table 2. For the sake of clarity, figure 11 shows the received signals, contour plot of the scalograms, and the line profile at the average

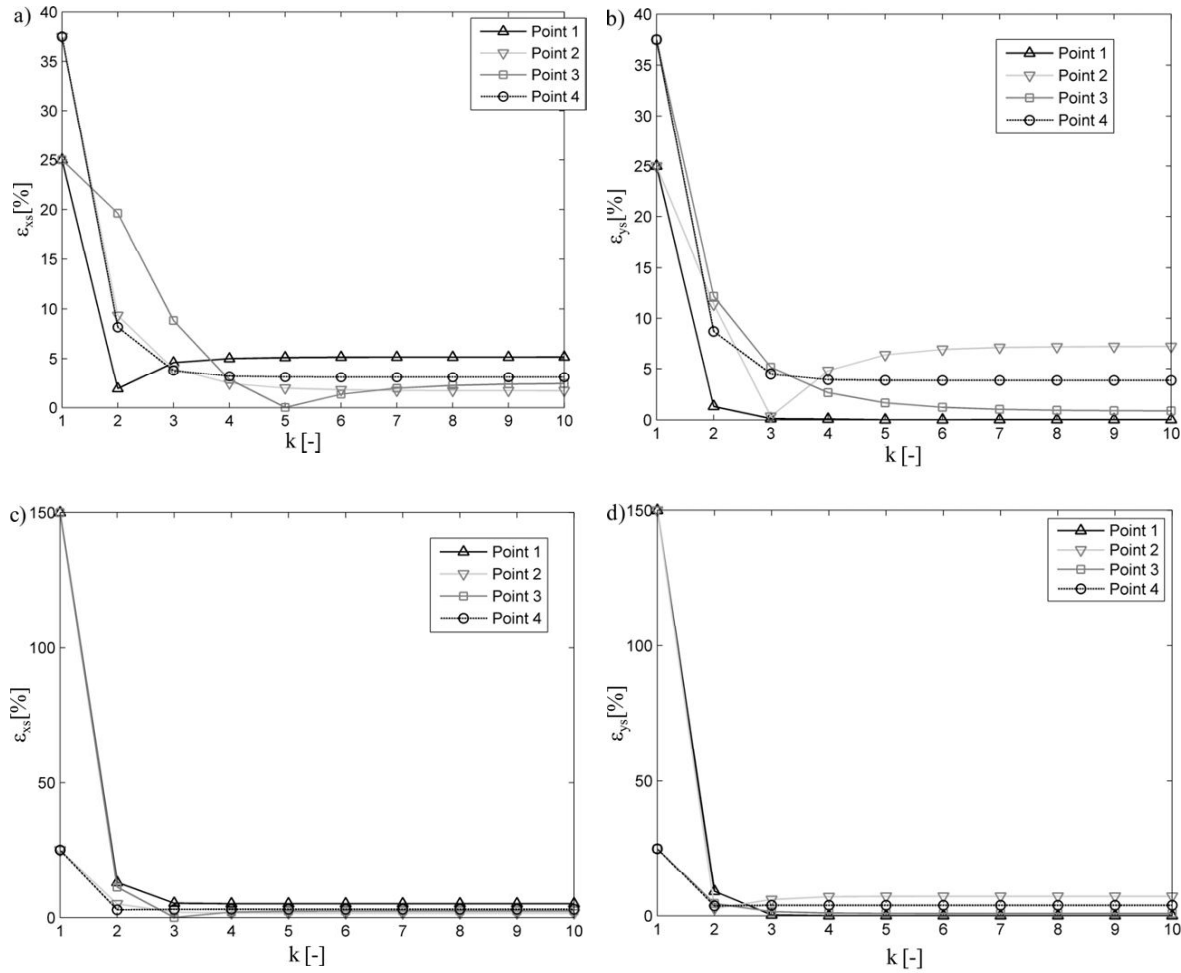


**Figure 14.** Source location error in the  $x$  and  $y$  coordinates using four sensors and considering as initial Gaussian locations: ((a), (b)) I; ((c), (d)) II; ((e), (f)) III, and ((g), (h)) IV.

frequency  $\bar{f} = 137$  kHz, for an AE source simulated at a given point (i.e. point #4) in the first sensor configuration setup. The transformation of the probability density function from the frequency domain to the group velocity domain has been shown in figure 6. The error of the estimated AE source location ( $\hat{x}_{sk}, \hat{y}_{sk}$ ) at the  $k$ th step can be defined as:

$$\varepsilon_{x_{sk}} = 100 \frac{|x_{sa} - \hat{x}_{sk}|}{|x_{sa}|} \% \quad (7.1)$$

$$\varepsilon_{y_{sk}} = 100 \frac{|y_{sa} - \hat{y}_{sk}|}{|y_{sa}|} \% \quad (7.2)$$

where  $(x_{sa}, y_{sa})$  are the coordinates of the actual source location. Figure 12 shows the results of the proposed approach using data from an array of three sensors (i.e. 1, 2, 4). In particular, the actual source location is marked as a squared dot ( $\square$ ). The estimated location, using the proposed algorithm, is represented on the figure by the symbol (+). It can be observed that using three sensors may lead to inaccurate estimation of source locations. In fact, the average errors of four simulated AE sources after 10 iterations in  $x$  and  $y$

directions according to equations (7.1) and (7.2) are 36% and 23%, respectively. Source location results obtained by adding the information provided by a fourth sensor, are illustrated in figure 13. In this case, the average errors after 10 iterations for  $x$  and  $y$  estimations are 4% and 5%, respectively. In general, the more information in hand the more accurate results can be obtained. Because of the matrix structure, the proposed method is very flexible in adding or removing the information from a network of sensors at the data processing stage. Furthermore, it is possible to consider different modes in the measurement vector. Indeed, if in addition to the antisymmetric  $A_0$ , the symmetric mode  $S_0$  is excited, the number of measurements increases from  $(n-1)$  to  $2(n-1)$ , with just one more unknown added to the state vector  $X$ , that is, the  $S_0$  group wave velocity. The convergence of the proposed approach using an array of four sensors is shown in figure 14. These results were obtained considering as a starting point the four initial Gaussian locations illustrated in figure 9. It can be observed that the proposed algorithm is capable of converging in just a few steps with an average error of less than 5% in both  $x$  and  $y$  coordinates, and in

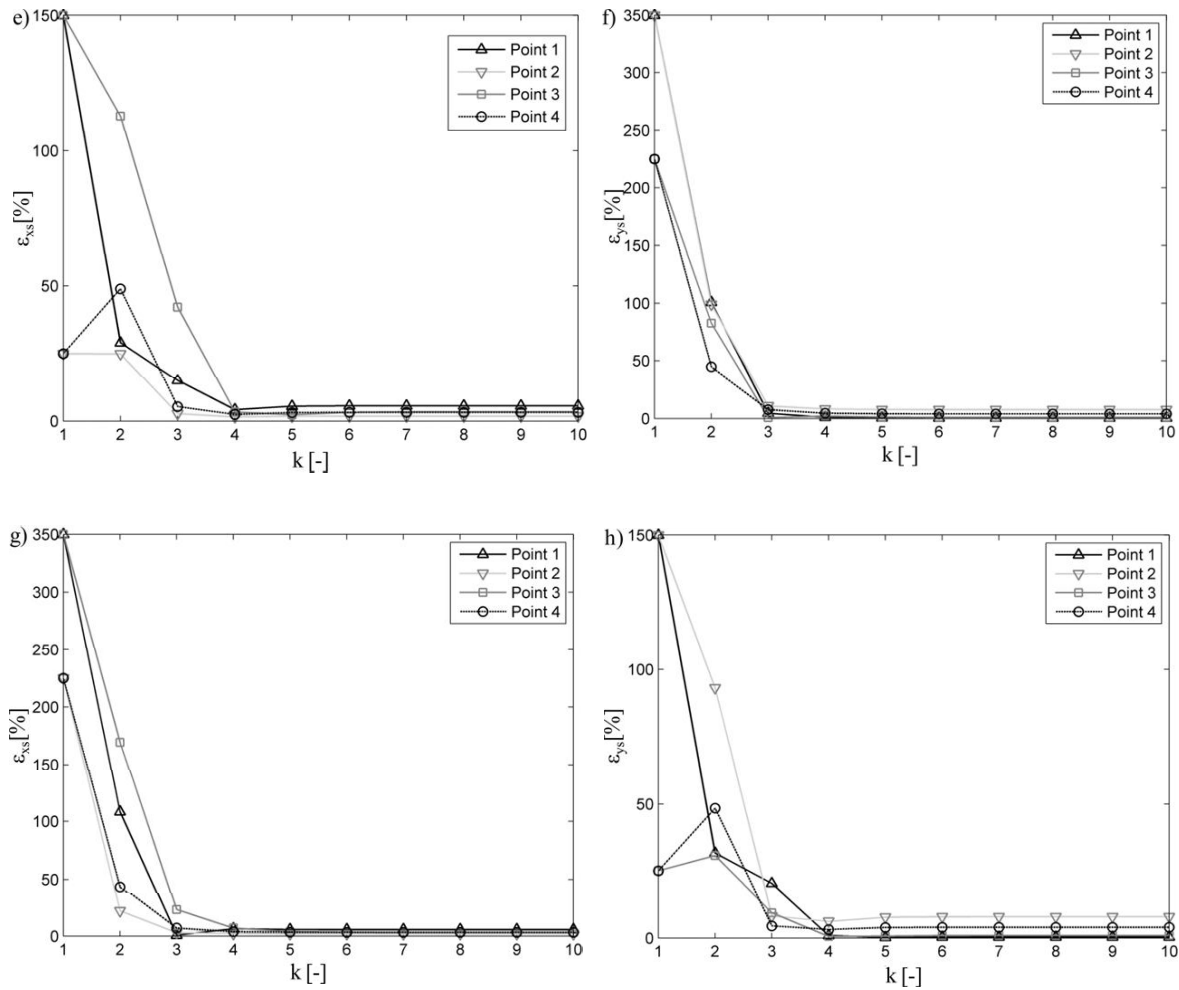


Figure 14. (Continued.)

**Table 3.** Actual and estimated source positions in the first setup configuration (with the first initial location).

Point no:	$x_s(\text{mm})^a$	$\hat{x}_s(\text{mm})$	$y_s(\text{mm})^a$	$\hat{y}_s(\text{mm})$	$\hat{V}_g(\text{m s}^{-1})$
1	50.8	47.01	50.8	49.7	2948.1
2	101.6	98.81	50.8	43.25	3022.4
3	50.8	48.61	101.6	100.5	2755.7
4	101.6	98.08	101.6	97.25	2883

Note: The origin of Cartesian coordinates is at sensor 1.

the worst case the error is less than 7.5%. It should be noted from figure 14, that the first Gaussian initial location can be considered as the worst scenario. In fact, although the first initial Gaussian location has the smallest starting error (i.e. it is closer to the actual locations), since the variance is small, the contribution of the correction stage is reduced; as a result the initial state tends to resist any correction or update. The results using the first initial Gaussian location are summarized in table 3. In addition, figure 14 demonstrates the robustness of the proposed approach to converging to the optimal solution in just six steps, regardless of the initial starting location.

Results obtained using the second configuration are shown in figure 15. The average errors in  $x$  and  $y$  are less

than 5% and 7% respectively. In this setup sensors cover the area 4.8 times the first configuration and the maximum distance between sensors is more than 560 mm. Table 4 summarizes, for each point, the results in terms of: actual location coordinates ( $x_{sa}$ ,  $y_{sa}$ ), estimated location coordinates ( $\hat{x}_s$ ,  $\hat{y}_s$ ), and estimated wave velocity  $\hat{V}_g$ .

Furthermore, an interesting feature of the proposed method is the capability to perform sensor and data fusion. Indeed, suppose that two techniques with different reliabilities are used during the first stage to perform time of arrival measurements, a decision should be made to combine the information according to their degree of reliability. The EKF is capable of fusing this information, so increasing the accuracy of the source location.

## 8. Conclusion

In this paper a probabilistic framework for locating acoustic emission sources is proposed based on the EKF theory. The proposed approach, in which TOF and wave velocity are considered as Gaussian random variables, consists of two main stages. During the first stage, TOF measurements of Lamb waves are carried out by a continuous wavelet



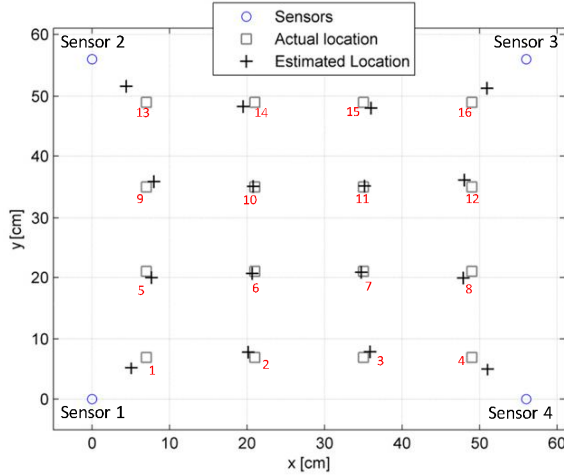


**Figure 15.** AE source localization results using four sensors in the second setup configuration.

**Table 4.** Actual and estimated source positions in the second configuration setup.

Point no:	$x_s$ (mm) <sup>a</sup>	$\hat{x}_s$ (mm)	$y_s$ (mm) <sup>a</sup>	$\hat{y}_s$ (mm)	$\hat{V}_g$ (m s <sup>-1</sup> )
1	70	50.53	70	51.25	3130.4
2	210	201.4	70	78.64	3121.8
3	350	358.7	70	79.16	3094.8
4	490	510.1	70	49.16	3110.8
5	70	76.73	210	199.6	3124.5
6	210	206.4	210	206.4	3117.6
7	350	347.1	210	208.5	3102.4
8	490	478.7	210	199.2	3142
9	70	79.83	350	358.5	3129.2
10	210	207.7	350	350.9	3127.5
11	350	351.5	350	351.5	3124.2
12	490	480.1	350	361.1	3087.7
13	70	44.05	490	516	3089.7
14	210	194.9	490	483.3	3101.7
15	350	359.7	490	480.8	3147.1
16	410	509.4	490	513.1	3129.4

Note: The origin of Cartesian coordinates is at sensor 1.

transform (CWT) accounting for systematic errors due to the Heisenberg uncertainty; the second stage uses the EKF to iteratively estimate the source location and the wave velocity. The advantages of the proposed algorithm over the traditional methods include the capability of: (1) taking into account uncertainties in TOF measurements and wave velocity and (2) efficiently fusing multi-sensor data to perform an efficient AE source localization. The proposed algorithm is computationally efficient and can be used in real-time applications. It should be noted that the signal processing stage (CWT) can be replaced by other methods capable of providing probabilistic measurement data for the estimation stage. The performance of the proposed algorithm has been validated through pencil-lead breaks performed on an aluminum plate at systematic grid locations. The plate was instrumented with an array of four piezoelectric transducers.

## Appendix

If the closed form solution of the group velocity as a function of frequency–thickness (equation (2.3)) is known, the probability density function of random variable  $V_g$  can be stated as:

$$P_{V_g}(V_g) = P_{fd}[F^{-1}(V_g)] \frac{dF^{-1}(V_g)}{dV_g} \quad (\text{A.1})$$

where  $P$  denotes the probability density function and  $d$  is the differential operator. Equation (A.1) is held if the function  $V_g = F(fd)$  is continuous and strictly monotonic [29]. It is well known that the Rayleigh–Lamb equation can be approximated, for low frequency–thickness by the plate theory for the two fundamental Lamb wave modes ( $S_0$  and  $A_0$ ) [40]. Under these conditions the phase velocities for  $S_0$  and  $A_0$  are expressed as:

$$V_{ph_{S_0}} = \sqrt{\frac{E}{\rho(1-\nu^2)}} \quad (\text{A.2})$$

$$V_{ph_{A_0}} = \left[ \frac{E(2\pi fd)^2}{12\rho(1-\nu^2)} \right]^{\frac{1}{4}} \quad (\text{A.3})$$

where  $\rho$ ,  $E$ , and  $\nu$  are density, Young’s modulus, and Poisson ratio respectively. The group velocity  $V_g$  can be calculated from the phase velocity  $V_{ph}$  according to the following equation [41]:

$$V_g = V_{ph}^2 \left[ V_{ph} - (fd) \frac{dV_{ph}}{d(fd)} \right]^{-1} \quad (\text{A.4})$$

The approximate group wave velocity of  $S_0$  and  $A_0$  can be expressed as:

$$V_{g_{S_0}} = \sqrt{\frac{E}{\rho(1-\nu^2)}} \quad (\text{A.5})$$

$$V_{g_{A_0}} = F(fd) = 2 \left[ \frac{E(2\pi fd)^2}{12\rho(1-\nu^2)} \right]^{\frac{1}{4}} \quad (\text{A.6})$$

More accurate approximation of  $A_0$  group velocity as an analytic function of frequency–thickness can be found in [42]. From equation (A.5) it is evident that the approximated  $S_0$  is not a function of frequency–thickness so the transformation of the probability density function of random variable  $fd$  to the approximated group wave velocity of  $S_0$  is not meaningful [28]. On the other hand from equation (A.6) it is obvious that the approximated group velocity for  $A_0$  is a continuous, strictly monotonic, and increasing function of  $fd$  so equation (A.1) is applicable in transferring the probability density function of random variable  $fd$  to  $V_{g_{A_0}}$ . Let us proceed with defining the inverse function of (A.6):

$$F^{-1}(V_{g_{A_0}}) = fd = \frac{V_{g_{A_0}}^2}{8\pi} \sqrt{\frac{12\rho(1-\nu^2)}{E}} \quad (\text{A.7})$$

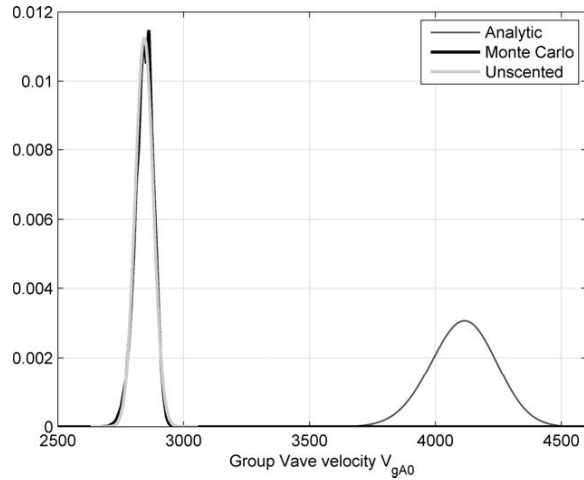


**Figure A.1.** Transformed probability density functions of random variable  $V_{gA_0}$  using analytic, Monte Carlo, and unscented methods.

The derivative of equation (A.4) is:

$$\frac{dF^{-1}(V_{gA_0})}{dV_{gA_0}} = \frac{V_{gA_0}}{4\pi} \sqrt{\frac{12\rho(1-\nu^2)}{E}}. \quad (\text{A.8})$$

If the probability density function of the random variable  $fd$  ( $P_{fd}(fd)$ ) is Gaussian with mean  $\bar{fd}$  and variance  $\sigma_{fd}^2$  the  $P_{fd}(fd)$  can be defined as:

$$P_{fd}(fd) = \frac{1}{\sigma_{fd}\sqrt{2\pi}} e^{-\frac{(fd-\bar{fd})^2}{2\sigma_{fd}^2}}. \quad (\text{A.9})$$

After substituting equations (A.7) and (A.8) into (A.1) and considering the  $P_{fd}(fd)$  stated in equation (A.9), the probability density function of  $V_{gA_0}$  is stated as:

$$P_{V_{gA_0}}(V_{gA_0}) = \left( \frac{1}{\sigma_{fd}\sqrt{2\pi}} e^{-\frac{\left(\frac{V_{gA_0}^2}{8\pi} \sqrt{\frac{12\rho(1-\nu^2)}{E}} - \bar{fd}\right)^2}{2\sigma_{fd}^2}} \right) \times \left( \frac{V_{gA_0}}{4\pi} \sqrt{\frac{12\rho(1-\nu^2)}{E}} \right). \quad (\text{A.10})$$

The probability density function of the approximated  $A_0$  Lamb group wave velocity is derived in equation (A.10). An alternative approach to perform this transformation is using a Monte Carlo simulation. However, although this is a reliable method, it is severely time consuming. To compare the performance of these three methods (analytic, Monte Carlo, and unscented transformation) data obtained from the AE source generated at the point 4 have been used, as shown in figure A.1. The Monte Carlo simulation has been carried out by randomly generating 200 000 samples from the random variable  $fd$  and the group wave velocity determined from equation (A.6). It can be observed that the unscented

transformation method is able to capture the probability density function of random variable  $V_{gA_0}$  just using three sigma points.

## References

- [1] Tan K 1995 Comparison of Lamb waves and pulse echo in detection of near-surface defects in laminate plates *NDT & E Int.* **28** 215–23
- [2] Ghosh T, Kundu T and Karpur P 1998 Efficient use of Lamb modes for detecting defects in large plates *Ultrasonics* **36** 791–801
- [3] Tua P S, Quek S T and Wang Q 2004 Detection of cracks in plates using piezo-actuated Lamb waves *Smart Mater. Struct.* **13** 643–60
- [4] Giurgiutiu V and Bao J 2004 Embedded-ultrasonics structural radar for *in situ* structural health monitoring of thin-wall structures *Struct. Health Monit.: Int. J.* **3** 121–40
- [5] Su Z and Ye L 2004 Fundamental Lamb mode-based delamination detection for CF/EP composite laminates using distributed piezoelectrics *Struct. Health Monit.: Int. J.* **3** 43–68
- [6] Mal A, Ricci F, Banerjee S and Shih F 2005 A conceptual structural health monitoring system based on vibration and wave propagation *Struct. Health Monit.: Int. J.* **4** 283–93
- [7] Kundu T, Das S and Jata K V 2007 Point of impact prediction in isotropic and anisotropic plates from the acoustic emission data *J. Acoust. Soc. Am.* **122** 2057–66
- [8] Kundu T, Das S, Martin S A and Jata K V 2008 Locating point of impact in anisotropic fiber reinforced composite plates *Ultrasonics* **48** 193–201
- [9] Salamone S, Bartoli I, Leo P D, Scalea F L D, Ajovalasit A, Acquisto L D, Rhymer J and Kim H 2010 High-velocity impact location on aircraft panels using macro-fiber composite piezoelectric rosettes *J. Intell. Mater. Syst. Struct.* **21** 887–96
- [10] Marchi L D, Marzani A, Speciale N and Viola E 2011 A passive monitoring technique based on dispersion compensation to locate impacts in plate-like structures *Smart Mater. Struct.* **20** 035021
- [11] Jeong H and Jang Y S 2000 Fracture source location in thin plates using the wavelet transform of dispersive waves *IEEE Trans. Ultrason. Ferroelectr. Freq. Control* **47** 612–9
- [12] Ciampa F and Meo M 2010 Acoustic emission source localization and velocity determination of the fundamental mode  $A_0$  using wavelet analysis and a Newton-based optimization technique *Smart Mater. Struct.* **19** 045027
- [13] Lu Y and Michaels J E 2005 A methodology for structural health monitoring with diffuse ultrasonic waves in the presence of temperature variations *Ultrasonics* **43** 717–31
- [14] Konstantinidis G, Drinkwater B W and Wilcox P D 2006 The temperature stability of guided wave structural health monitoring systems *Smart Mater. Struct.* **15** 967–76
- [15] Croxford A J, Wilcox P D, Drinkwater B W and Konstantinidis G 2007 Strategies for guided-wave structural health monitoring *Proc. R. Soc. A* **463** 2961–81
- [16] Lanza di Scalea F and Salamone S 2008 Temperature effects in ultrasonic Lamb wave structural health monitoring systems *J. Acoust. Soc. Am.* **124** 161–74
- [17] Salamone S, Bartoli I, Lanza di Scalea F and Coccia S 2009 Guided-wave health monitoring of aircraft composite panels under changing temperature *J. Intell. Mater. Syst. Struct.* **20** 1079–90
- [18] Clarke T, Simonetti F and Cawley P 2010 Guided wave health monitoring of complex structures by sparse array systems: Influence of temperature changes on performance *J. Sound Vib.* **329** 2306–22

- [19] Marioli D, Narduzzi C, Offelli C, Petri D, Sardini E and Taroni A 1991 Digital time of flight measurement for ultrasonic sensors *IMTC-91: Instrumentation and Measurement Technology Conf. Conference Record. 8th IEEE (May)* pp 198–201
- [20] Seydel R and Chang F K 2001 Impact identification of stiffened composite panels: I. System development *Smart Mater. Struct.* **10** 354–69
- [21] Haywood J, Coverley P T, Staszewski W and Worden K 2005 An automatic impact monitor for a composite panel employing smart sensor technology *Smart Mater. Struct.* **14** 265–71
- [22] Leclerc J, Worden K, Staszewski W and Haywood J 2007 Impact detection in an aircraft composite panel—A neural-network approach *J. Sound Vib.* **299** 672–82
- [23] Kundu T, Das S and Jata K V 2009 Detection of the point of impact on a stiffened plate by the acoustic emission technique *Smart Mater. Struct.* **18** 035006
- [24] Hajzargerbashi T, Kundu T and Bland S 2011 An improved algorithm for detecting point of impact in anisotropic inhomogeneous plates *Ultrasonics* **51** 317–24
- [25] Gaul L 1998 Identification of the impact location on a plate using wavelets *Mech. Syst. Signal Process.* **12** 783–95
- [26] Gaul L, Hurlebaus S and Jacobs L 2001 Localization of a synthetic acoustic emission source on the surface of a fatigue specimen *Res. Nondestruct. Eval.* **13** 105–17
- [27] Coverley P T and Staszewski W 2003 Impact damage location in composite structures using optimized sensor triangulation procedure *Smart Mater. Struct.* **12** 795–803
- [28] Auld B A 1973 *Acoustic Fields and Waves in Solids* (New York: Wiley)
- [29] Soong T T 2004 *Fundamentals of Probability and Statistics for Engineers* (New York: Wiley)
- [30] Kishimoto K, Inoue H, Hamada M and Shibuya T 1995 Time frequency analysis of dispersive waves by means of wavelet transform *J. Appl. Mech.* **62** 841–6
- [31] Mallat S 1998 *A Wavelet Tour of Signal Processing* (London: Academic)
- [32] Meo M, Zumpano G, Piggott M and Marengo G 2005 Impact identification on a sandwich plate from wave propagation responses *Compos. Struct.* **71** 302–6
- [33] Tse N C F and Lai L L 2007 Wavelet-based algorithm for signal analysis *EURASIP J. Adv. Signal Process.* **2007**
- [34] Crassidis J L and Junkins J L 2004 *Optimal Estimation of Dynamic Systems* (Boca Raton, FL: Chapman & Hall/CRC Applied Mathematics & Non-linear Science)
- [35] Sabatini A M 1995 A digital signal-processing technique for compensating ultrasonic sensors *IEEE Trans. Instrum. Meas.* **44** 869–74
- [36] Tsai C C 1998 A localization system of a mobile robot by fusing dead-reckoning and ultrasonic measurements *IEEE Trans. Instrum. Meas.* **47** 1399–404
- [37] Moreno V M and Pigazo A 2009 *Kalman Filter: Recent Advances and Applications* In-Teh
- [38] Julier S, Uhlmann J and Durrant-whyte H F 2000 A new method for the nonlinear transformation of means and covariances in filters and estimators *IEEE Trans. Autom. Control* **45** 477–82
- [39] Prosser W H, Gorman M R and Humes D H 1991 AE source orientation by plate wave analysis *J. Acoust. Emiss.* **9** 283–8
- [40] Shull P J 2001 *Nondestructive Evaluation Theory, Techniques, and Applications* (New York: Dekker)
- [41] Rose J L 2004 *Ultrasonic Waves in Solid Media* (Cambridge: Cambridge University Press)
- [42] Hayashi Y, Ogawa S, Cho H and Takemoto M 1999 Non-contact estimation of the thickness and elastic properties of metallic foils by wavelet transform of laser generated lamb waves *NDT & E Int.* **32** 21–7